Grain boundary serration tuning and its effect on hot workability of a wrought superalloy

Tso-Wei Chen, Pei-Te Wang, Yung-Chang Kang, Bo-Cheng Wu, Nien-Ti Tsou, Uwe Glatzel, Stéphane Gorsse, An-Chou Yeh

Grain boundary serration tuning and its effect on hot workability of a wrought superalloy

Tso-Wei Chen[1, 2], Pei-Te Wang[3], Yung-Chang Kang[4], Po-Cheng Wu[5], Nien-Ti Tsou[3], Uwe Glatzel[6], Stéphane Gorsse[7], An-Chou Yeh[1, 2, 8*]

[1] Ph.D. Program in Prospective Functional Materials Industry, National Tsing Hua University, 101, Sec. 2, Kuang-Fu Road, Hsinchu, 30013, Taiwan R.O.C.

[2] High Entropy Materials Center, National Tsing Hua University, 101, Sec. 2, Kuang-Fu 10 Road, Hsinchu, 30013 Taiwan R.O.C.

[3] Department of Materials Science and Engineering, National Yang Ming Chiao Tung University, Hsinchu, 30010, Taiwan R.O.C.

[4] Gloria Material Technology Corporation, 10, Gong 2nd Road, Liuying District, Tainan. 73659, Taiwan R.O.C.

[5] S-Tech Corporation, 15, Gong 1st Road, Environmental Science and Technology Park, Liouying District, Tainan. 73659, Taiwan R.O.C.

[6] Metals and Alloys, University of Bayreuth, Prof.-Rüdiger-Bormann-Str. 1, 95447, Bayreuth, Germany

[7] CNRS, Univ. Bordeaux, Bordeaux INP, ICMCB, UMR 5026, F-33600, Pessac, France

[8] Department of Materials Science and Engineering, National Tsing Hua University, 101, Sec. 2, Kuang-Fu Road, Hsinchu, 30013, Taiwan R.O.C.

*Corresponding Author: yehac@mx.nthu.edu.tw

Abstract

This study aims to elucidate the underlying mechanism of grain boundary serration and investigate its effects on hot workability of U720Li superalloy. Industrial scale as-cast ingots were subjected to heat treatments with varying cooling rates (15°C/s, 0.1°C/s, 0.02°C/s and 0.003°C/s) prior hot deformation. With 15°C/s cooling process, samples possessed straight boundaries and fine $L1_2$ structured γ' particles dispersion. When the cooling rate was decreased to 0.1°C/s and below, coarsened γ' particles could pin grain boundaries and lead to undulation in morphology. Continuous and discontinuous precipitation of γ' phase were both associated with the formation of grain boundary serration. And, two types of grain boundary serrations were identified, the first type (Type-I) was associated with an average interparticle spacing of 1.31 μm, and the second type (Type-II) was related to an average interparticle spacing of 5.98 μm. Discontinuous formation of long strip γ' behind the mobile grain boundary was observed for Type-II boundary, and it exhibited larger degree of undulation than that of Type-I boundary. With increasing fractions of Type-II boundary, the hot formability of U720Li was significantly improved during compression tests at 1000 °C. With grain boundary serration, the sample could be compressed up to 70% reduction ratio (1.2 strain) without crack formation. Analysis indicates that straight grain boundaries were prone to formation of cavitation and intergranular crack. On the other hand, serrated grain boundaries could distribute the strain evenly and inhibit crack propagation. This work presents a simple approach to improve the hot deformability of U720Li fabricated by industrial facility.

Keywords: superalloys; heat treatment; serrated grain boundary; isothermal compression

1. Introduction

Udimet-720Li is an advanced nickel-based superalloy with excellent creep, fatigue, oxidation and corrosion resistances [1-4], it is utilized mainly for the turbine disk application in aerospace engines [3]. The industrial production of U720Li disk is primarily based on powder metallurgy process, since the alloy contains high fraction of strengthening precipitates ($L1_2$ structured γ' phase) to resist high temperature deformation, thermos-mechanical production process can be very challenging [5-7]. Nevertheless, plastic deformation of U720Li has remained a subject of interest to-date due to continuing industrial demands to lower down the processing cost. A relatively narrow hot working window between 1100°C and 1150°C has been proposed by previous studies [3,8,9], at temperatures just below 1100°C, large amount of γ' precipitation could increase the flow stress and result strain localization, typically the reduction ratios couldn't reach over 50% without severe crack formation [10,11]. On the other hand, intergranular fracture could occur at high temperatures above the γ' solvus temperature (about 1150 °C) and cause a limited reduction ratio of 30% [12,13]. Fahrmann et al. [14] reported that the cross sectional reduction ratio of U720Li could reach 60% by controlling the cooling rate from an annealing temperature of 1110°C to a testing temperature of 1010 °C with 3 °C/s in order to prevent the formation of secondary γ'. In another study, an increase in carbon content from 0.014 to 0.071 wt% could promote dynamic recrystallization, which could result softening mechanism and delay crack formation during hot deformation [10]; a reduction ratio of 45% was achieved at 1060 °C.

Serrated grain boundary is known to inhibit grain boundary sliding and retard crack propagation [15-27]. It can also provide resistance against hydrogen-induced intergranular crack formation and propagation in nickel-based alloys [15]. Several studies have reported that serrated grain boundary can be induced by heat treatment with slow cooling process to promote interaction between grain boundaries and second phases, such as γ' [16-19,25], δ [23], $M_{23}C_6$-carbide [22]…etc. For Inconel718, precipitation and growth of δ phase could result zigzag grain boundary morphology, and it was found to increase creep resistance under 650 °C/625 MPa condition and prolong the creep life by 400 h [23]. Serrated grain boundary induced by the precipitation of MC-carbide in IN600 could improve creep life and creep strain under 815 °C/70 MPa [26]. For Astrology, crack propagation rate during fatigue test at 750 °C was notably decreased by a factor of about 3 to 5 due to grain boundary serration [25]. The formation of serrated grain boundary in U720Li alloy has also been reported in previous study [27], it was found to increase the Charpy impact energy by 25 J and prolong creep life by 250 h under 704 °C/690 MPa. Koul et al. [16] proposed that the net strain energy difference between the coherent matrix and incoherent side of γ' precipitate along grain boundary could cause grain boundary serration. Mitchell et al. [18] observed the preferential growth of γ' precipitates to induce protrusions along the grain boundaries in RR1000 alloy. Qiu et al.[19] studied the microstructures of RR1000 alloy and proposed that grain boundary migration could be pinned by the coarsened γ' precipitates during slow cooling to result periodic wavy grain boundary structures. Based on existing literatures of grain boundary serration in Ni-based alloys, continuous precipitation and coarsening of the γ' phase were the main attributing factors to grain boundary serration, although discontinuous precipitation of γ' precipitates in stripe form was also reported, this feature has not yet analyzed and discussed in details [18]. This study aims to investigate the underlying mechanism for the formation of serrated grain boundary of U720Li alloy with respect to both continuous and discontinuous precipitations of γ', and most importantly this work is the first to investigate the effect of grain boundary serration on hot formability at 1000ºC, which is below the lower

boundary of the proposed hot working temperatures in between 1100ºC~1150ºC; findings in this work can provide a guideline to design wrought processing route for high strength superalloys such as U720Li.

2. Materials and methods

In this work, U720Li was supplied by Gloria Material Technology Corporation, Taiwan (R.O.C.), an ingot was fabricated by the industrial scale vacuum induction melting (VIM furnace, Consarc corp.) followed by vacuum arc remelting process (V700, Consarc corp.); the size of ingot was 580 mm in diameter and 1200 mm in length. Chemical compositions were measured in different parts of the ingot by X-Ray fluorescence (XRF, Axios FAST PW4600, Malvern Panalytical Ltd), spark optical emission spectrometer (Spark-OES, ARL3460, Thermo Fisher Scientific Inc.) and carbon and sulfur determinator (CS844ES, LECO corp.). The chemical composition in weight percentage is shown in table. 1.

Table. 1. Chemical composition of as-received U720Li (in wt. %).

Al	Co	Cr	Mo	Ni	Ti	W	Others (ppm)
2.55 ± 0.05	14.72 ± 0.02	16.42 ± 0.06	2.97 ± 0.02	57.20 ± 0.27	4.88 ± 0.01	1.24 ± 0.02	B: 135 ± 2 C: 65 ± 2 Zr: 289 ± 7

In order to design heat treatment, samples of U720Li ingot were subjected to differential scanning calorimeter analysis (DSC, STA PT 1750C, Linseis Inc.). Measurements were conducted at a heating rate of 10 °C/s, the DSC curve is shown in Figure 1; the solidus temperature and γ' solvus are 1280 °C and 1155 °C, respectively.

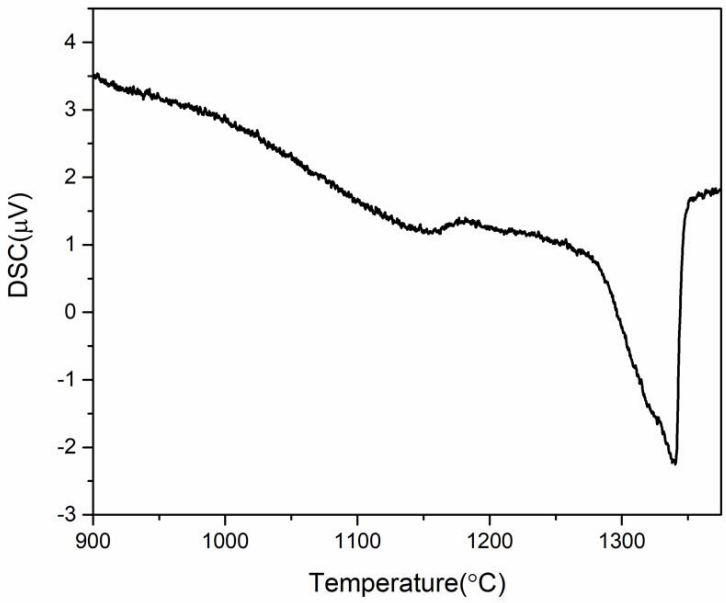

Figure. 1. DSC heating curve of the U720Li ingot.

Cylindrical specimens, 8mm in diameter and 12mm in height, were machined by electro-discharge

machining. In order to ensure the consistency of microstructure and chemical composition, all of the specimens were machined from a half radius of the ingot. Figure 2 shows the heat treatment profiles in the present study. Homogenization treatment was conducted to minimize elemental segregation, and the temperature was chosen at 1180 °C for 16 h to fully dissolve the γ' phase. Different cooling rates (15 °C/s, 0.1 °C/s, 0.02 °C/s and 0.003 °C/s in average) were conducted to an intermediate temperature at 950 °C followed by air cooling. The 15 °C/s cooling process was achieved by air cooling and the cooling rate was measured by recording the temperature change using K-type thermocouple. The other three cooling processes (0.1 °C/s, 0.02 °C/s and 0.003 °C/s) were achieved by setting the time course of temperature changes of the heating furnace. HT-1, HT-2, HT-3, and HT-4 are designated for samples subjected to 4 different heat treatment profiles, Figure 2.

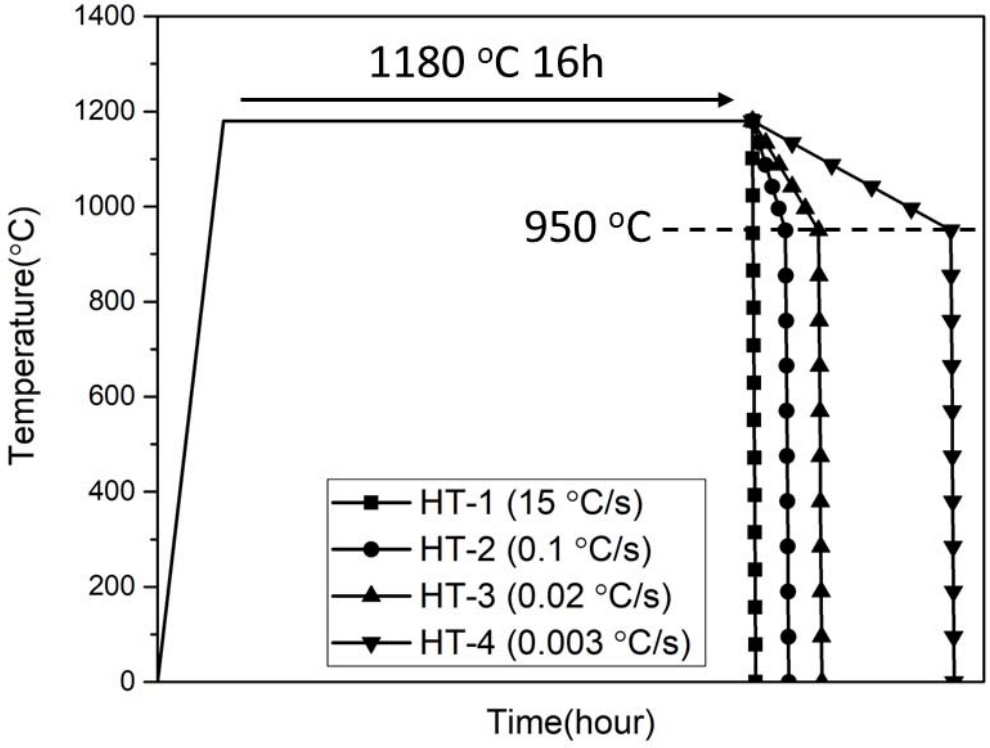

Figure. 2. Heat treatment profiles in present work

Isothermal compression tests were conducted on specimens using Gleeble-3500 thermal-mechanical machine (Dynamic Systems Incorporation) at the Industrial Technology Research Institute, Taiwan. Prior to deformation, the samples were heated up to working temperature at a heating rate of 10 °C/s and then held for 5 min to ensure temperature uniformity. The specimens were then compressed at 1000 °C with a strain rate of 0.1 s^{-1}. Specimens were also subjected to compression to 15% reduction ratio (0.16 strain) in order to analyze the early stage of deformation.

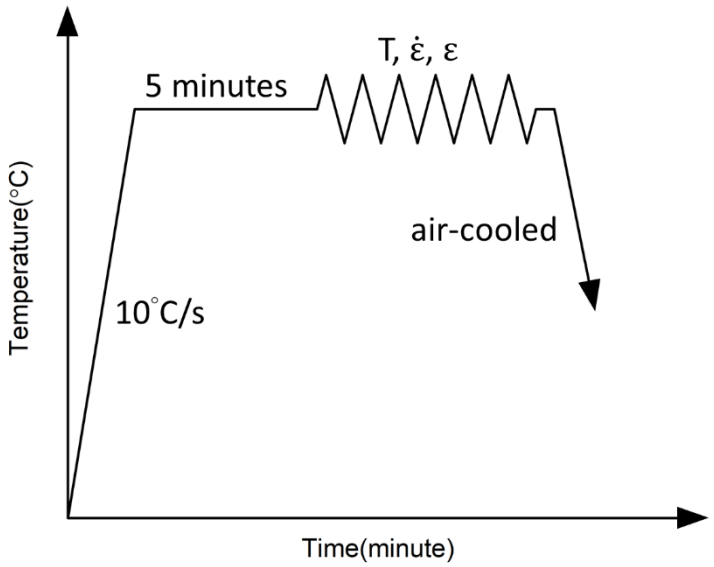

Figure. 3. Isothermal compression tests.

Microstructure observations were conducted by using scanning electron microscopy (SEM, JEOL JSM-IT100 and Zeiss Gemini 300) and optical microscopy (OM, Olympus BX-51M). Metallographic samples were prepared using grinding and polishing methods. The specimens were electrolytically polished with 20% H_3PO_4 in C_2H_5OH at 2V for 5s; to reveal grain boundaries, chemical etchant Kallings reagent was used (5g CuCl2+ 100ml HCl+ 100ml C_2H_5OH). The quantification of precipitates and the geometric characteristics of grain boundaries were analyzed by ImageJ software [28]. Compressed specimens were sectioned parallel to the compression axis to analyze the deformed microstructure. EBSD analysis was conducted to investigate internal strain distribution and recrystallization behavior by Zeiss Gemini 300 scanning electron microscope equipped with Symmetry S2 EBSD detector and Aztec Crystal software.

Molecular dynamic (MD) simulation was conducted to simulate different strain distributions along triple junctions of straight and serrated grain boundaries. The polycrystalline model of pure nickel was established by Atomsk [29]. The model includes 43256710 atoms in total with a size of 80 x 80 x 80 nm^3. It is worth noting that the 3-dimensional surface profile of serrated grain boundaries was built by scanning the EBSD figures with Dream.3D [30]. Then, periodic boundary conditions along the x, y, and z directions of the model were applied to reduce the amount of computation. The interatomic interactions in this model were described by 2NN MEAM potentials[31,32]. The temperature of the models was equilibrated at 1000 ºC for 120 ps with the timestep of 2fs to achieve a thermodynamic equilibrium. The model was then compressed along the y direction at a constant strain rate of 10^{-3} s^{-1}. The isothermal-isobaric NPT ensemble was used in both the above-mentioned processes. The molecular dynamics simulations were calculated by LAMMPS[33] and the corresponding results were post-processed by OVITO [34]. The Voronoi analysis modifier [35] and the common neighbor analysis (CNA)[36] were used here to reveal volumetric strain and crystal structures in the models, respectively.

3. Results

3.1 Heat treated microstructures prior hot deformation

The microstructure of the as-melted U720Li is shown in Fig. 4(a), it contained coarse grains with dendritic structure; the average grain size was 772 μm. After the homogenization heat treatment, the dendrites were all eliminated. In HT-1 sample, fast cooling after homogenization treatment produced straight grain boundaries (Fig. 4(b)), and the average grain size was 1150 μm. With the cooling rate reduced to 0.1 °C/s, the grain boundary turned from straight to serrated morphology in HT-2 sample (Fig. 4(c)), and the average grain size was 1280 μm. Further decrease in cooling rate to 0.02 °C/s resulted more pronounced serrated grain boundaries (Fig. 4(d)), the average grain size of HT-3 sample was 1290 μm. More undulation of grain boundary was observed with cooling rate about 0.003 °C/s (Fig, 4(e)); cellular structures were identified around the serrated grain boundaries, the average grain size of HT-4 sample was 1580 μm.

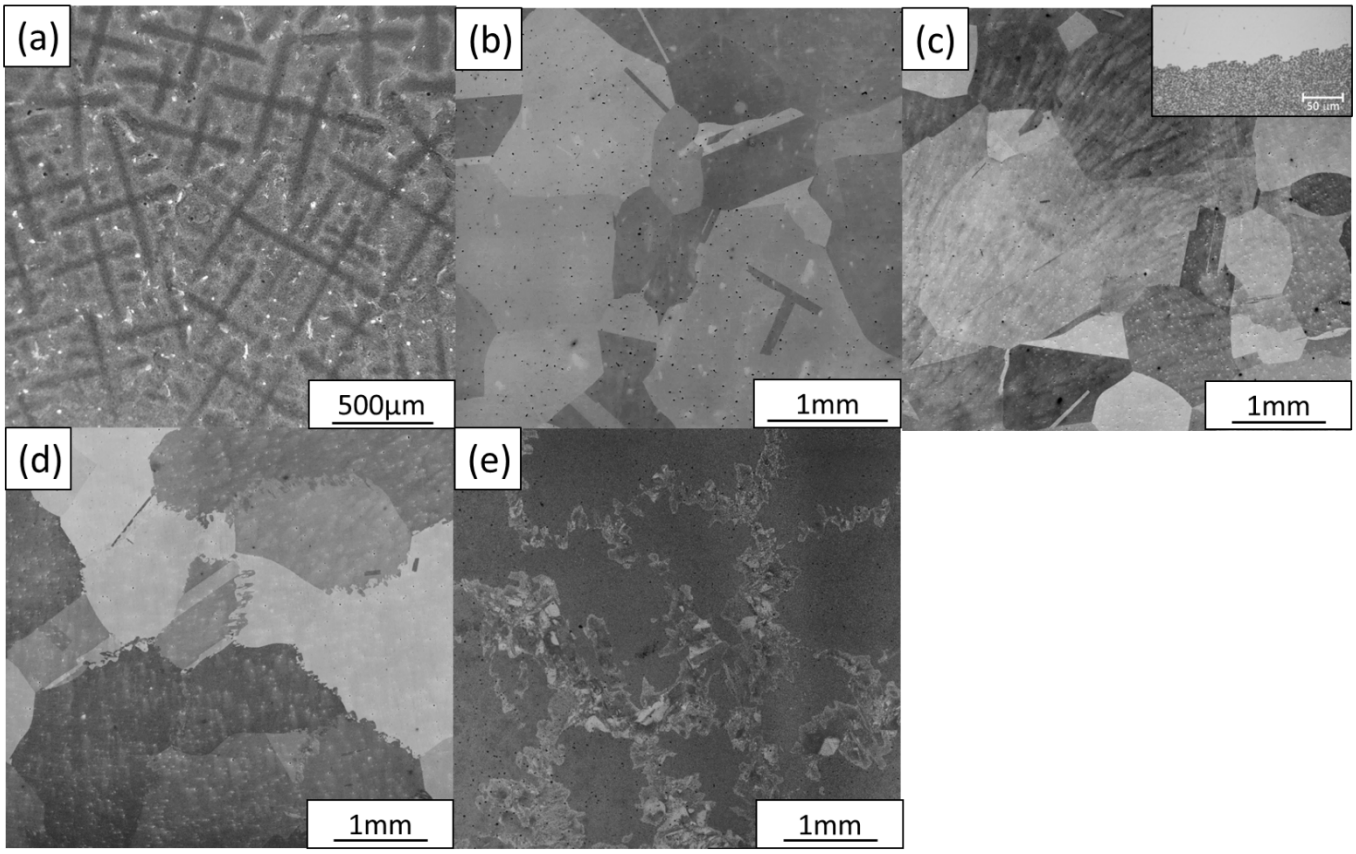

Figure. 4. OM image showing macroscopic grain structures of (a) as-cast, (b) HT-1 sample, (c)HT-2 sample, (d) HT-3 sample and (e) HT-4 sample.

Fig. 5. reveals that both size and distribution of γ' precipitates were affected by the cooling rates after heat treatment. The 15 °C/s cooling process in HT-1 sample resulted fine dispersion of γ' particles (Fig. 5(a)), the average γ' diameter was 113 nm and the average interparticle spacing was 0.27 μm. Slower cooling rates yielded larger particles with lower number density and larger interparticle spacing (Fig. 5(b, c, d)). The average γ' diameter of HT-2, HT-3 and HT-4 samples was 444, 662 and 1208 nm, and the average interparticle spacing was 1.31, 2.19 and 5.98 μm, respectively. Furthermore, cellular precipitates were observed in HT-3 and HT-4 samples (Fig. 5(e, f)), this phenomenon was associated with discontinuous

precipitation of γ’ at the front of mobile grain boundary during slow cooling processes.

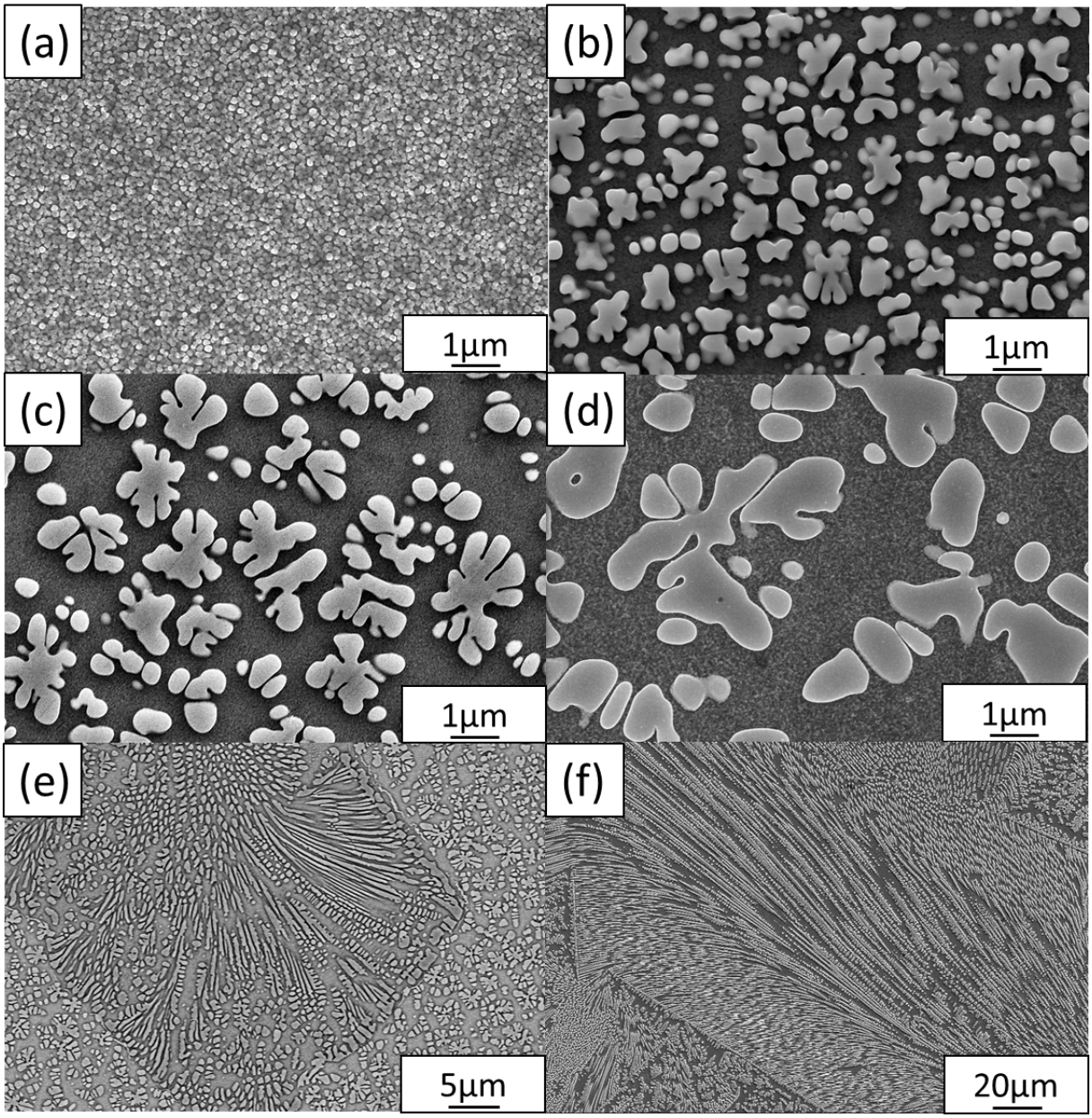

Figure. 5. SEM image showing γ’ precipitates of (a) HT-1, (b) HT-2, (c) HT-3, (d) HT-4 specimens and cellular precipitates in (e) HT-3, (f) HT-4 specimens.

Fig. 6. shows that continuous precipitation and discontinuous precipitation of γ’ phase were both associated with grain boundary serration during slow cooling process. Continuous precipitation of coarsened γ’ particles could pin grain boundaries and lead to a small degree of undulation, this is termed as the Type-I boundary. On the other hand, further reduction in cooling rate could further coarsen the particles and widen the interspacing in-between the γ’ particles to an extent that enabled segments of mobile grain boundary to bend through the supersaturated matrix in-between the particles, and resulted the formation of cellular structure, which is known as the discontinuous precipitation [37]; this type of grain boundary migration process resulted a larger degree of grain boundary undulation than that of Type-I, and this is termed as the Type-II boundary in this work. The effect of cooling rates on γ’ particle size and interparticle spacing is shown in Fig. 7(a).

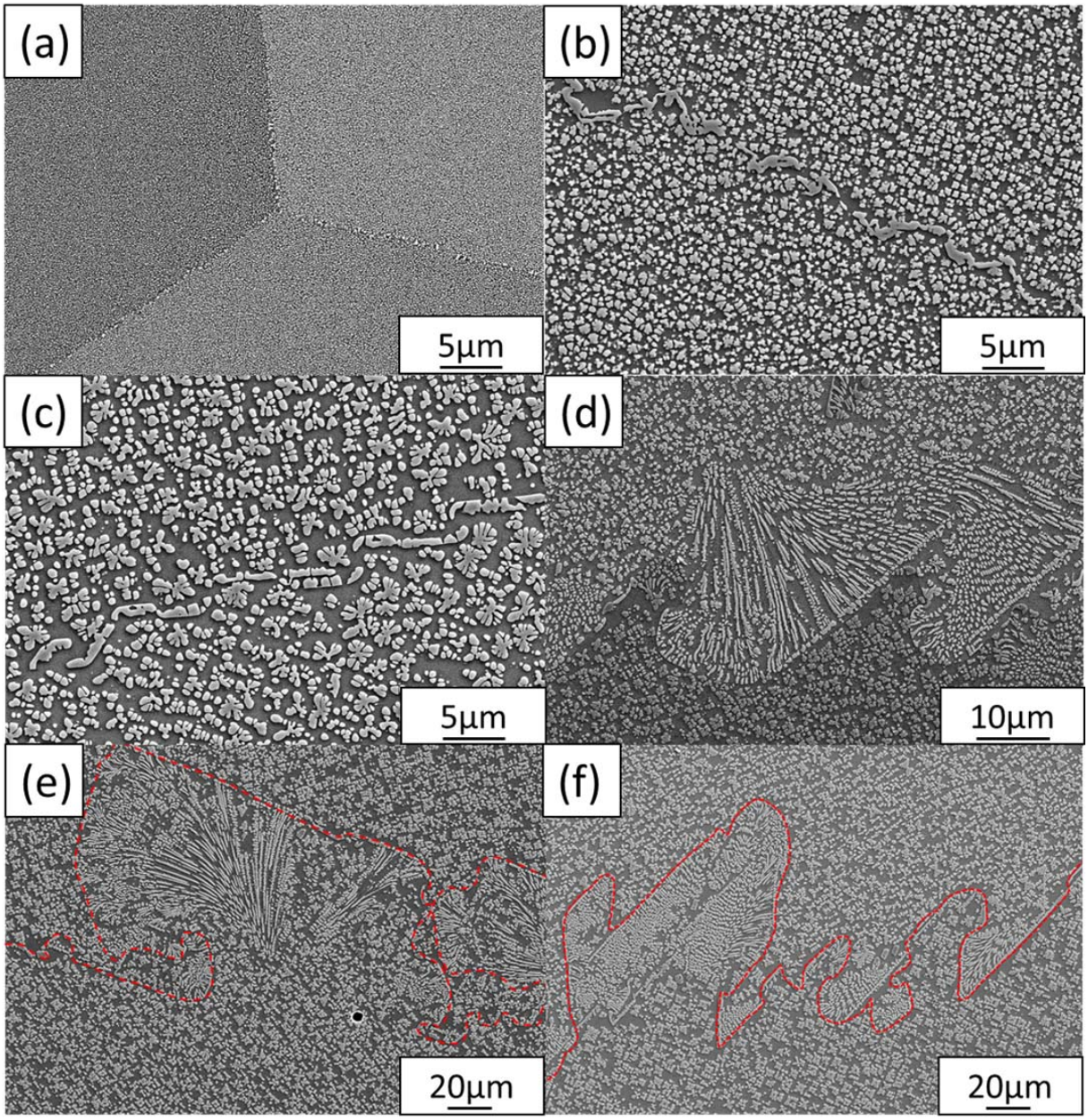

Figure. 6. SEM image showing (a) straight boundary in HT-1 sample, CP-type boundary in (b)HT-2 sample, (c) HT-3, DP-type boundary in (d) HT-3 sample, (e), (f) HT-4 sample.

The correlation between fractions of two different types of serrated grain boundaries versus the undulation of grain boundaries is quantified in Fig. 7(b). HT-2 sample consisted of 93.94% of Type-I boundary, the amplitude of its serrated structures was about 1.37 µm. Further decrease in cooling rate could promote higher fractions of Type-II boundaries, thus the undulation of grain boundary serration would be more pronounced. HT-3 sample contained 76.20% of Type-II boundary, the fraction of Type-II boundary was further increased to 99.13% in HT-4 sample. Aa a result, the amplitude of the grain boundary increased from 29.16 µm to 135.27 µm.

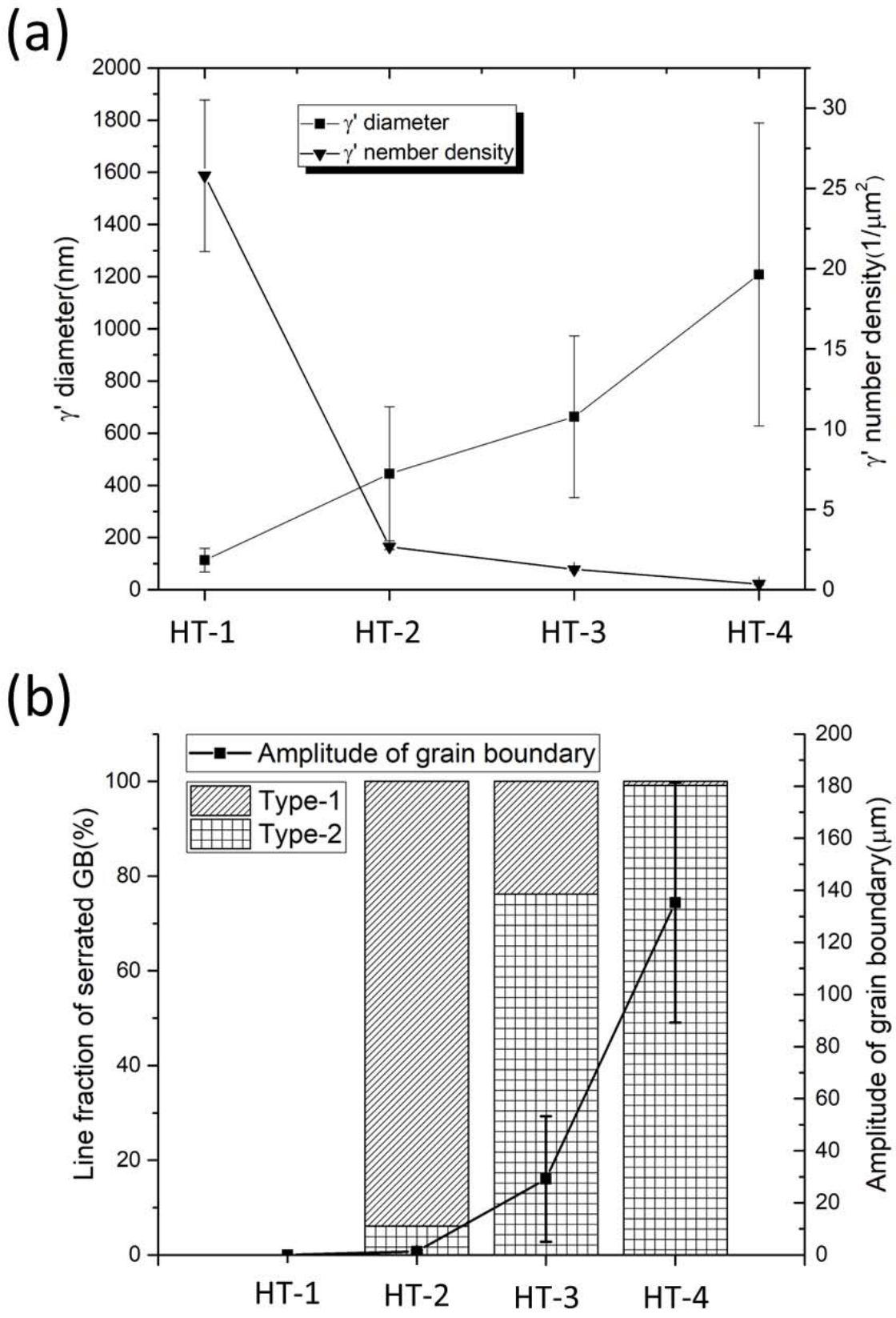

Figure. 7. (a) Average diameter and number density of γ' phase in four different specimens, (b) The correlation between fractions of two different types of serrated grain boundaries versus the amplitude in four different specimens.

3.2 Hot deformation behaviors and microstructure analysis

Fig. 8 shows the true stress-strain curves of four different specimens compressed at 1000 °C with a strain rate of 0.1 s^{-1}; photographs of the deformed specimens are also shown. The stress-strain data presented are prior the formation of crack, which could lead to a sharp drop in flow stress. HT-1 sample possessed higher flow stress comparing with the others due to fine dispersion of small γ' particles; the yield strength of HT-1 sample was about 333.61MPa. With further decrease in cooling rate, coarsened γ' particles resulted a decrease in yield strength of HT-2, HT-3 and HT-4 samples to be about 283.41, 270.54 and 249.49 MPa, respectively. Most importantly, the hot formability of U720Li was improved with decreasing cooling rate. Cracks occurred in HT-1 sample after a reduction ratio around 20% (0.22 strain), several cracks could be observed on sample surface (Fig. 8(b)). For HT-2 sample, the hot ductility was improved moderately with Type-I serrated grain boundary, and cracks were observed at 31% reduction ratio (0.37 strain) (Fig. 8(c)). HT-3 sample with 76.20% of Type-II boundary could endure more deformation up to 45% reduction ratio (0.6 strain). HT-4 sample with 100 % Type-II serrated grain boundary could be compressed to 70% reduction ratio (1.2 strain) without crack formation (Fig. 6(e)). The result suggests that hot formability was significantly improved by inducing Type-II grain boundary serration.

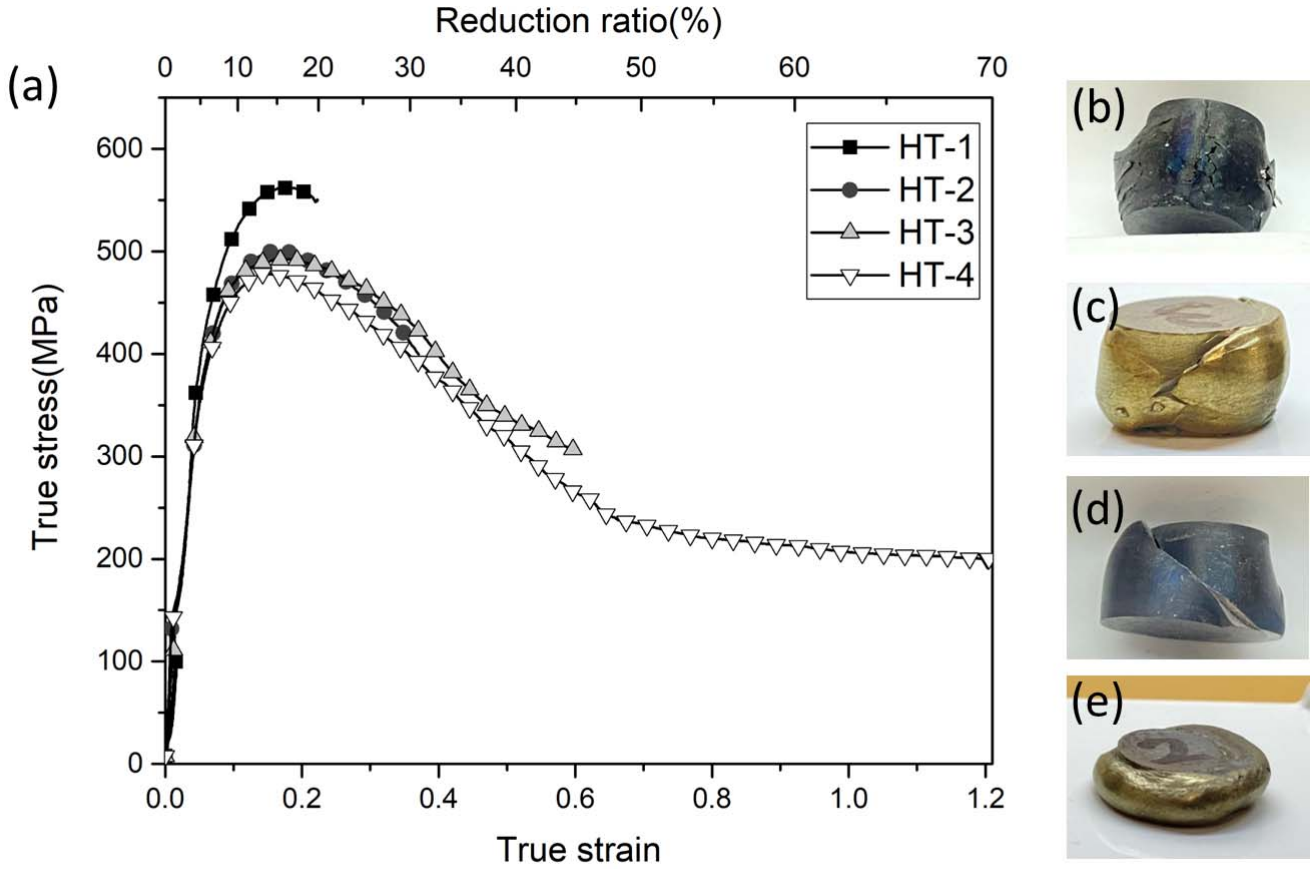

Figure. 8. (a) Stress-strain curve of four specimens tested at 1000 °C with a strain rate of 0.1s^{-1} and the macroscopic view of deformed samples (b) HT-1, (c) HT-2, (d) HT-3, (e) HT-4.

Microstructures of deformed samples were examined, and intergranular cracks were identified in HT-1, HT-2 and HT-3 samples (Fig. 9). The microstructure of the HT-1 sample shows large intergranular cracks

along the straight grain boundary (Fig. 9(a)). Fig. 9(b) and 9(c) show several intergranular cracks in HT-2 sample. In HT-3 sample, intergranular cracks could only be observed on the Type-I boundary and no cracks were seen along Type-II boundary (Fig. 9(d) and 9(e)). The HT-4 sample, which consisted of 100% Type-II boundary, could be deformed to 70% reduction ratio without crack formation (Fig. 9(f)).

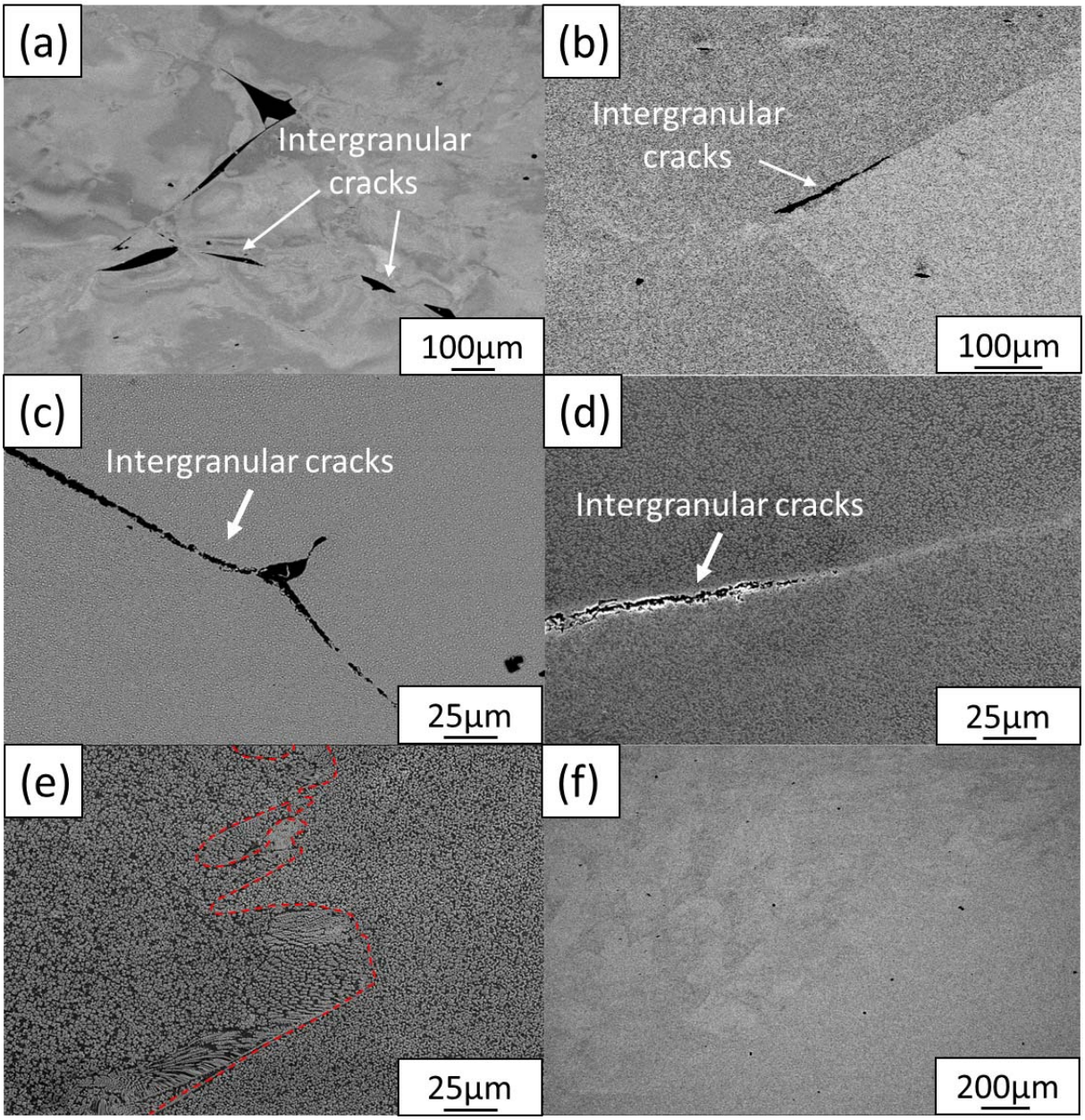

Figure. 9. SEM images showing compressed microstructures of (a) HT-1, (b, c) HT-2, (d, e) HT-3, (f) HT-4.

Furthermore, recrystallizations were observed in all tested samples. Figure. 10 shows the inverse pole figure (IPF) maps of four compressed specimens. Only a small number of recrystallized grains were observed in HT-1 sample (see Fig. 10(a)). The recrystallized grain fraction was increased in HT-2 sample (see Fig. 10(b)), and this was due to a higher amount of strain. Recrystallized grains were found to develop from grain boundary surroundings toward the grain interior in HT-3 sample (see Fig. 10(c)). A fully recrystallized grain structure was identified in HT-4 sample compressed to 70% reduction ratio (see Fig. 10(d)), the recrystallized grain size was about 2μm in average.

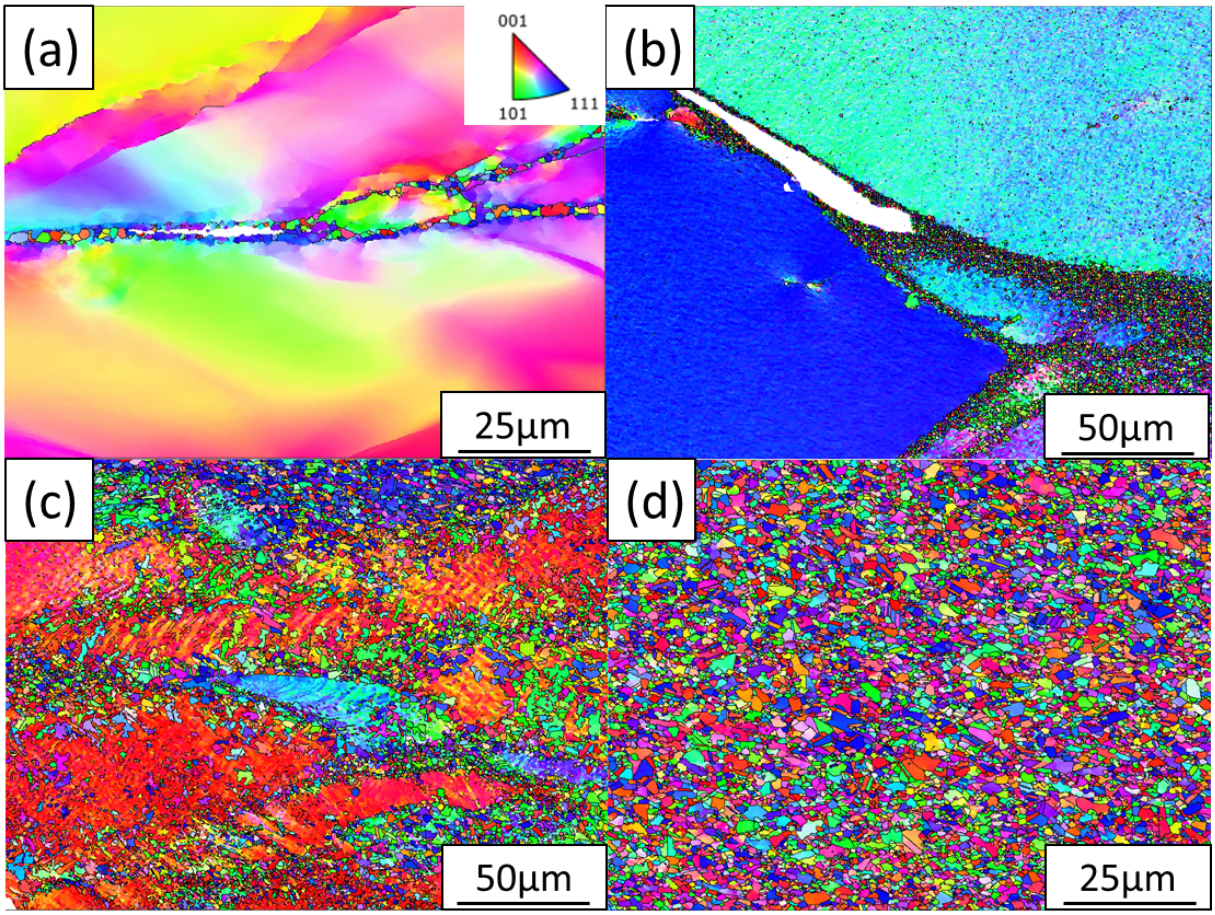

Figure. 10. IPF maps of (a) HT-1 compressed to 20% reduction ratio (0.22 strain), (b) HT-2 compressed to 31% reduction ratio (0.37 strain), (c) HT-3 compressed to 45% reduction ratio (0.6 strain), (d) HT-4 sample compressed to 70% reduction ratio (1.2 strain) at 1000 °C and 0.1 s^{-1}.

The formation of Type-II boundary is associated with the formation of cellular structure. Microstructural analysis shows that cellular structure could be deformed without crack formation under 1000 ºC (Fig. 11 (a)). EBSD analysis showed dynamic recrystallization occurred in the γ matrix between the coarse γ', and regions around the cellular structure showed finer recrystallized grains with size about 800 nm in average (as shown in the red circle in Fig. 11(b) & (c)).

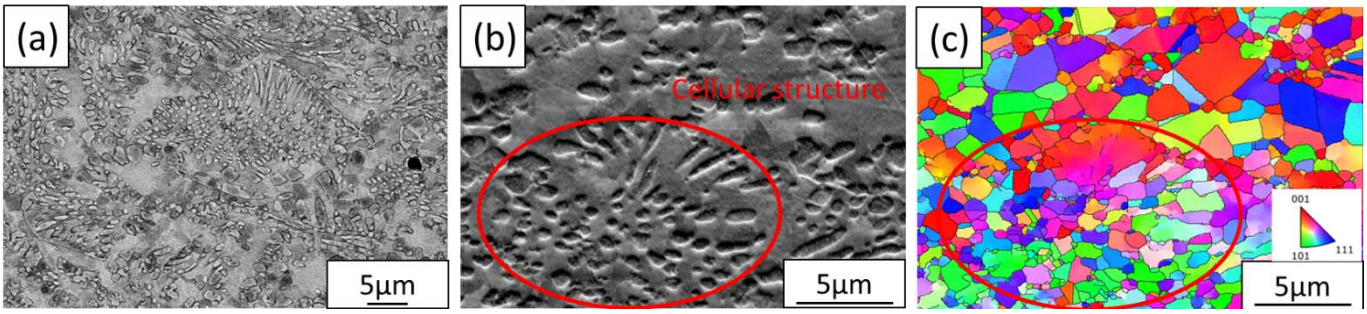

Figure. 11. (a) SEM image, (b) EBSD forward scatter diodes(FSD) image and its corresponding (c) IPF image showing the compressed microstructure in HT-4 sample deformed at 1000°C and 0.1s^{-1} to 70% reduction ratio (1.2 strain).

In order to examine internal strain under the same reduction ratio for different types of grain boundary, specimens of HT-1, HT-2, HT-3 and HT-4 were compressed to 15% reduction ratio at 1000 °C, and microstructures were analyzed by EBSD. Fig. 12 shows the IPF maps and the kernel average misorientation (KAM) maps. In HT-1 sample, high local misorientation was found to concentrate at grain boundary triple junction (Fig. 12(b)), this could lead grain boundary cavitation and crack propagation with further deformation. In HT-2 sample, local misorientation was found to distribute more uniformly along the Type-I serrated grain boundary instead of concentrating at the triple junction (Fig. 12(d)). Type-II boundaries could exhibit higher degree of undulation than that of Type-I boundaries and resulted a more uniform stress distribution throughout the microstructure (Fig. 12(f) and 12(h)), so samples with higher fractions of Type-II boundaries could withstand higher degree of deformation since sample could be uniformly deformed.

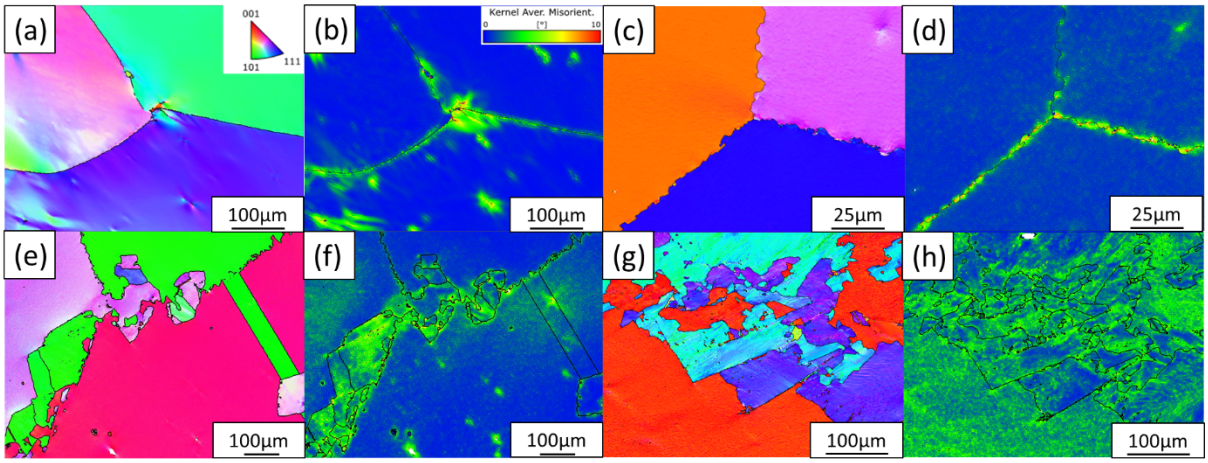

Figure. 12. IPF and KAM maps of (a), (b) HT-1, (c), (d) HT-2, (e), (f) HT-3, (g), (h), HT-4 sample tested at 1000°C with a strain rate of 0.1 s^{-1} to 15% reduction ratio (0.16 strain).

4. Discussions

In this study, formation of serrated grain boundary and its effect on hot deformation behavior in U720Li alloy has been investigated. Grain boundary serration can be induced in U720Li during solution heat treatment with cooling rate of 0.2 °C/s and below, continuous and discontinuous precipitation of γ' phase could both affect grain boundary serration, causing the Type-I and Type-II serration, respectively. The schematic illustrations of two different mechanisms are shown in Fig. 13. Type-I boundary would occur due to grain boundary pinning by coarse γ' particles (Fig. 13(a)). Type-II boundary would form due to the discontinuous precipitation behind the moving grain boundary, in order to relax the metastable state of supersaturated matrix, boundary migration accompanied by cellular precipitation can lead to large boundary undulation (as shown in Fig. 13(b)). As a lower cooling rate reduces the nucleation rate of γ', coarse precipitates with low number density and high particle interspacing are produced. This provides more space for grain boundaries to migrate freely and allows grain boundaries to pass through more supersaturated matrix. Therefore, discontinuous reaction is enhanced with reducing cooling rate, resulting in a higher fraction of cellular structure and more distorted grain boundary structure; the average amplitude of serrated grain boundary increased dramatically from 1.37 µm (HT-2 sample) to 135.27 µm (HT-4 sample) due to a 93% increment of the fraction of Type-II

boundary.

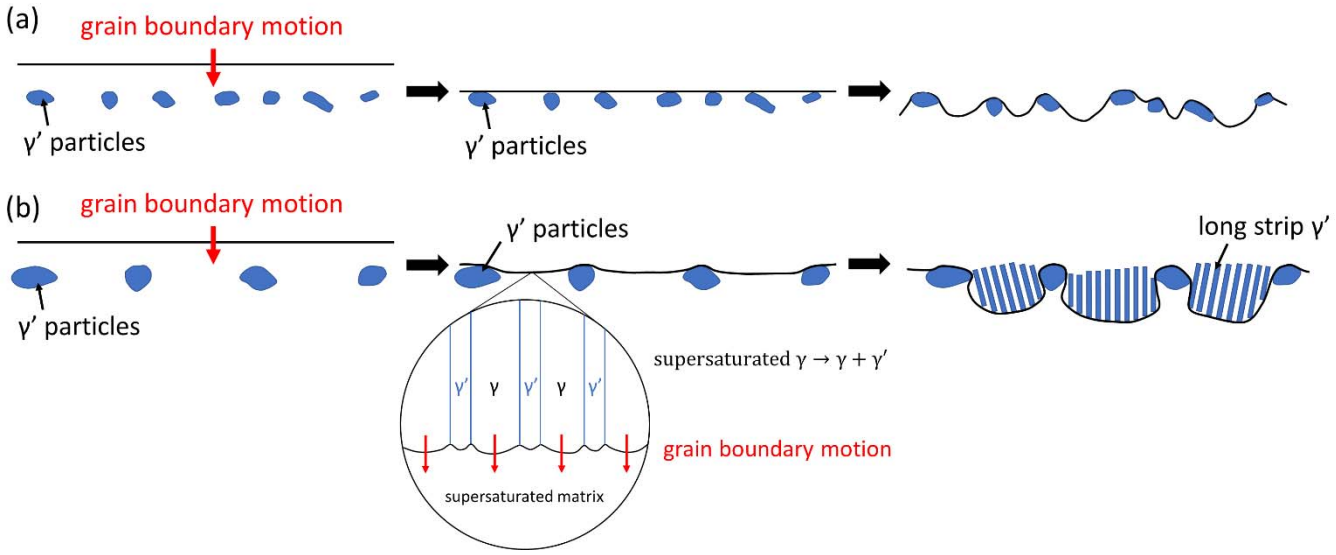

Figure. 13. Schematic illustration of the formation of (a) Type-I and (b) Type-II serrated grain boundary.

According to the results of compression test (Figure 8), HT-1 sample exhibited highest yield strength at 1000 °C, and the strength decreased with reducing cooling rate. The precipitation strengthening of γ' particles is mainly contributed by dislocation shearing based on the weak-pair and strong-pair coupling mechanism [38]. In the present study, different sizes of γ' particles are generated under four different heat treatments. And based on previous study [39], dislocation shearing of these four sizes of γ' in Udimet720Li alloy are all dominated by strong-pair coupling mechanism. The following equation describes the critical resolved shear stress:

$$\sigma_{strong-pair\ coupling} = \frac{1}{2} 1.72 \frac{T f^{\frac{1}{2}} w}{bd} \left(1.28 \frac{d\gamma_{APB}}{wT} \right)^{\frac{1}{2}}$$

where γ_{APB} is the anti-phase boundary energy (~0.243 J/m^2 at 1000°C[38]), b is Burgers vector(~0.257nm calculated from Thermo-Calc software [40]), f is the volume fraction of the particle(~33% at 1000°C), d is the particle diameter, w is a constant describing the repulsion between the pair dislocations and is approximately equal to 1, T is the line tension of the dislocation equal to $Gb^2/2$, and G is the elastic shear modulus(~55.1GPa at 1000°C calculated using simple pair-wise mixture model [41]). The critical resolved shear stress of the HT-1 specimen was calculated to be 133.71 MPa, which is about 65.28, 73.37, and 90.89MPa higher than HT-2, HT-3, and HT-4 specimens, respectively. This is comparable with the difference in yield strength measured from the compression test results, suggesting that the flow stress difference in four specimens is mainly due to the difference in γ' strengthening effect.

This study shows that grain boundary morphologies strongly influence the hot formability of U720Li alloy; the serrated morphology could help to reduce the occurrence of stress concentration (see Fig. 12(d)). Type-II grain boundary allows a more uniform deformation, as the EBSD results show that the lattice misorientation distributed more uniformly with reducing cooling rate (Fig. 12). Therefore, HT-4 sample with mostly Type-II boundaries showed a ductility improvement over 50% reduction ratio. To clarify the effect of grain boundary morphology on hot deformation behavior, MD simulations of isothermal compression tests

have been conducted; the simulated strain distribution are shown in Fig. 14. During deformation, strains distributed more intensely on the straight boundaries and the triple junctions showed highly localized strain (as shown in the red circle in Fig. 14(a)). The average volumetric strain around the triple junction was about 26.02%. While this phenomenon was not observed in serrated grain boundary structure, in contrast, it showed a much uniform strain distribution along the grain boundary (Fig. 14(b)), and the average volumetric strain at triple junction was only about 12.04%. This result confirms that serrated grain boundaries can effectively reduce stress concentration on grain boundary junctions.

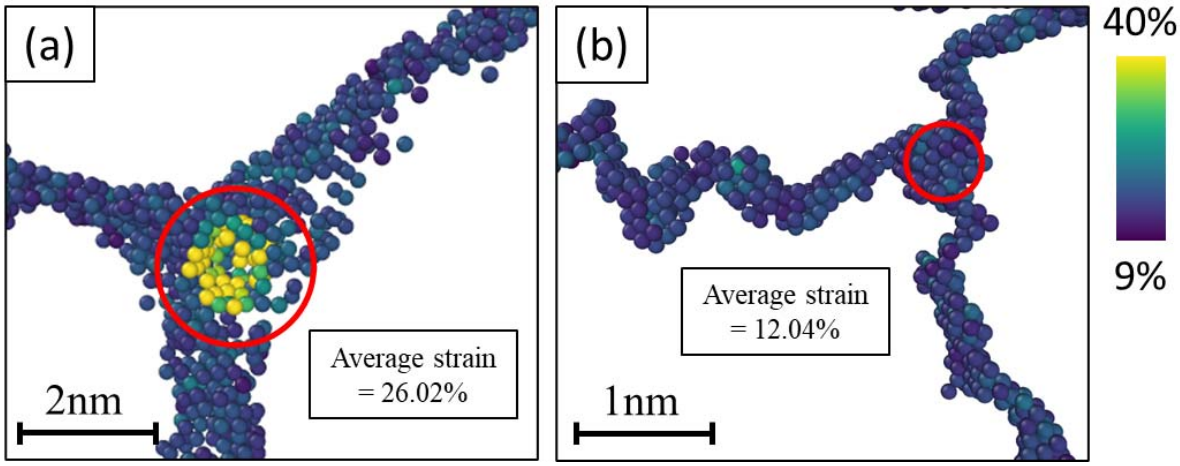

Figure. 14. MD simulation of strain distribution along (a) straight grain boundary and (b) serrated grain boundary compressed at 1000 ºC to about 6% strain.

Plastic deformation provides the driving force for the initiation of dynamic recrystallization. Since grain boundary is the preferred nucleation site of recrystallization, pronounced necklace structure is formed on the straight grain boundary in HT-1 sample (Fig. 10(a, b)). Recrystallized grains can further nucleate at the interface between recrystallized and deformed regions when the pre-existing grain boundaries are all covered with recrystallized grains. Therefore, recrystallized grains could gradually develop into the original grain interior with further deformation and finally reach fully recrystallization (see Fig. 10(d)). Interestingly, cellular structure could be plastically deformed during compression at 1000 ºC. Dynamic recrystallization was confined within the γ matrix and limited by the presence of coarse γ'. Since cellular structure consists of strip γ', fine recrystallized grain structure was developed around the cellular structure than the grain interior (see Fig. 11(c)). This work presents the underlying mechanism for the formation of serrated grain boundary of U720Li alloy with respect to both continuous and discontinuous precipitations of γ', and most importantly this work is the first to investigate the effect of grain boundary serration on hot formability at 1000ºC, which is below the lower boundary of the proposed hot working temperatures in between 1100ºC~1150ºC; findings in this work provides a guideline to design wrought processing route for high strength superalloys such as U720Li.

5. Conclusions

The underlying mechanism of grain boundary serration of an advanced superalloy made by industrial scale furnace has been elucidated in this work, as-cast ingots were subjected to heat treatments with varying

cooling rates (15°C/s, 0.1°C/s, 0.02°C/s and 0.003°C/s) prior hot deformation. With 15°C/s cooling process, samples possessed straight boundaries and fine $L1_2$ structured γ' particles dispersion. When the cooling rate was decreased to 0.1°C/s and below, coarsened γ' particles could pin grain boundaries and lead to undulation in morphology. Continuous and discontinuous precipitation of γ' phase were both associated with the formation of grain boundary serration. And, two types of grain boundary serrations were identified, Type-I was associated with an average interparticle spacing of 1.31 μm, and Type-II was related to an average interparticle spacing of 5.98 μm. Discontinuous formation of long strip γ' behind the mobile grain boundary was observed for Type-II boundary, and it exhibited larger degree of undulation than that of Type-I boundary. With increasing fractions of Type-II boundary, the hot formability of the superalloy was significantly improved during compression tests at 1000 °C. With grain boundary serration, the sample could be compressed up to 70% reduction ratio (1.2 strain) without crack formation. Analysis indicates that straight grain boundaries were prone to formation of cavitation and intergranular crack, and serrated grain boundaries could distribute the strain evenly and inhibit crack propagation.

Acknowledgments

Authors would like to acknowledge funding support from Gloria Material Technology Corporation and S-Tech Corporation. This work was also financially supported by the "High Entropy Materials Center" from The Featured Areas Research Center Program within the framework of the Higher Education Sprout Project by the Ministry of Education (MOE) and from the Project NSTC 111-2634-F-007-008,111-2224-E-007-003,110-2221-E-007-020-MY3 by National Science and Technology Council (NSTC) in Taiwan.

References

1. Evans, W.J.; Jones, J.P.; Williams, S. The interactions between fatigue, creep and environmental damage in Ti 6246 and Udimet 720Li. *International Journal of Fatigue* **2005**, *27*, 1473-1484, doi:https://doi.org/10.1016/j.ijfatigue.2005.06.029.
2. Marchionni, M.; Osinkolu, G.A.; Onofrio, G. High temperature low cycle fatigue behaviour of UDIMET 720 Li superalloy. *International Journal of Fatigue* **2002**, *24*, 1261-1267, doi:https://doi.org/10.1016/S0142-1123(02)00043-9.
3. Sczerzenie, F.; Maurer, G. Development of Udimet 720 for High Strength Disk Applications. *Superalloys 1984* **1984**, doi:10.7449/1984/Superalloys_1984_573_580.
4. Chen, J.H.; Rogers, P.M.; Little, J.A. Oxidation behavior of several chromia-forming commercial nickel-base superalloys. *Oxidation of Metals* **1997**, *47*, 381-410, doi:10.1007/BF02134783.
5. Alloy, W.; Bryant, D.; Mcintosh, G. THE MANUFACTURE AND EVALUATION OF A LARGE TURBINE. 1996.
6. Furrer, D.; Fecht, H. Ni-based superalloys for turbine discs. *JOM* **1999**, *51*, 14-17, doi:10.1007/s11837-999-0005-y.
7. Couturier, R.; Burlet, H.; Terzi, S.; Dubiez, S.; Guetaz, L.; Raisson, G. Process Development and Mechanical Properties of Alloy U720LI for High Temperature Turbine Disks. *Proceedings of the Tenth International Symposium on Superalloys,[S. l.][sn]* **2004**, 351-359, doi:10.7449/2004/Superalloys_2004_351_359.

8. Qu, J.-l.; Bi, Z.-n.; Du, J.-h.; Wang, M.-q.; Wang, Q.-z.; Zhang, J. Hot Deformation Behavior of Nickel-Based Superalloy GH4720Li. *Journal of Iron and Steel Research, International* **2011**, *18*, 59-65, doi:https://doi.org/10.1016/S1006-706X(12)60023-5.
9. Wan, Z.; Hu, L.; Sun, Y.; Wang, T.; Li, Z. Hot deformation behavior and processing workability of a Ni-based alloy. *Journal of Alloys and Compounds* **2018**, *769*, 367-375, doi:https://doi.org/10.1016/j.jallcom.2018.08.010.
10. Zhao, G.; Zang, X.; Jing, Y.; Lü, N.; Wu, J. Role of carbides on hot deformation behavior and dynamic recrystallization of hard-deformed superalloy U720Li. *Materials Science and Engineering: A* **2021**, *815*, 141293, doi:https://doi.org/10.1016/j.msea.2021.141293.
11. Li, Z.; Fu, S.H.; Wang, T.; Zhao, Y.X.; Zhang, Y.; Zhang, M.C. Microstructure Evolution and Processing Map of Superalloy GH720Li during Isothermal Compression. *Materials Science Forum* **2013**, *747-748*, 588-593, doi:10.4028/www.scientific.net/MSF.747-748.588.
12. Fan, H.; Jiang, H.; Dong, J.; Yao, Z.; Zhang, M. An optimization method of upsetting process for homogenized, nickel-based superalloy Udimet 720Li ingot considering both cracking and recrystallization. *Journal of Materials Processing Technology* **2019**, *269*, 52-64, doi:https://doi.org/10.1016/j.jmatprotec.2019.01.013.
13. Monajati, H.; Karimi Taheri, A.; Jahazi, M.; Yue, S. Deformation characteristics of isothermally forged UDIMET 720 nickel-base superalloy. *Metallurgical and Materials Transactions A: Physical Metallurgy and Materials Science* **2005**, *36*, 895-905, doi:10.1007/s11661-005-0284-z.
14. Fahrmann, M.; Suzuki, A. EFFECT OF COOLING RATE ON GLEEBLE HOT DUCTILITY OF UDIMET ALLOY 720 BILLET. *Superalloys* **2008**, 311-316.
15. Zhao, M.; Hu, H.; Rong, L. Heat treatment method for realizing grain boundary sawtooth of iron-nickel-based alloy. CN110484702B, 20190730 2019.
16. Koul, A.K.; Gessinger, G.H. On the mechanism of serrated grain boundary formation in Ni-based superalloys. *Acta Metallurgica* **1983**, *31*, 1061-1069, doi:https://doi.org/10.1016/0001-6160(83)90202-X.
17. Koul, A.K.; Thamburaj, R. Serrated grain boundary formation potential of Ni-based superalloys and its implications. *Metallurgical Transactions A* **1985**, *16*, 17-26, doi:10.1007/BF02656707.
18. Mitchell, R.J.; Li, H.Y.; Huang, Z.W. On the formation of serrated grain boundaries and fan type structures in an advanced polycrystalline nickel-base superalloy. *Journal of Materials Processing Technology* **2009**, *209*, 1011-1017, doi:https://doi.org/10.1016/j.jmatprotec.2008.03.008.
19. Qiu, C.L.; Andrews, P. On the formation of irregular-shaped gamma prime and serrated grain boundaries in a nickel-based superalloy during continuous cooling. *Materials Characterization* **2013**, *76*, 28-34, doi:https://doi.org/10.1016/j.matchar.2012.11.012.
20. Tanaka, M.; Iizuka, H.; Ashihara, F. Effects of serrated grain boundaries on the crack growth in austenitic heat-resisting steels during high-temperature creep. *Journal of Materials Science* **1988**, *23*, 3827-3832, doi:10.1007/BF01106799.
21. McQueen, H.J.; Ryan, N.D.; Konopleva, E.V.; Xia, X. Formation and application of grain boundary serrations. *Canadian Metallurgical Quarterly* **1995**, *34*, 219-229, doi:https://doi.org/10.1016/0008-4433(95)00001-E.

22. Hong, H.U.; Kim, I.S.; Choi, B.G.; Kim, M.Y.; Jo, C.Y. The effect of grain boundary serration on creep resistance in a wrought nickel-based superalloy. *Materials Science and Engineering: A* **2009**, *517*, 125-131, doi:https://doi.org/10.1016/j.msea.2009.03.071.
23. Yeh, A.-C.; Lu, K.-W.; Kuo, C.-M.; Bor, H.-Y.; Wei, C.-N. Effect of serrated grain boundaries on the creep property of Inconel 718 superalloy. *Materials Science and Engineering: A* **2011**, *530*, 525-529, doi:https://doi.org/10.1016/j.msea.2011.10.014.
24. Kim, H.P.; Choi, M.J.; Kim, S.W.; Kim, D.J.; Lim, Y.S.; Hwang, S.S. Effect of serrated grain boundary on stress corrosion cracking of Alloy 600. *Nuclear Engineering and Technology* **2018**, *50*, 1131-1137, doi:https://doi.org/10.1016/j.net.2018.05.009.
25. Danflou, H.L.; Marty, M.; Walder, A. FORMATION OF SERRATED GRAIN BOUNDARIES AND THEIR EFFECT ON THE MECHANICAL PROPERTIES IN A P/M NICKEL BASE SUPERALLOY. *Superalloys* **1992**, 63-72.
26. Tang, Y.T.; Wilkinson, A.J.; Reed, R.C. Grain Boundary Serration in Nickel-Based Superalloy Inconel 600: Generation and Effects on Mechanical Behavior. *Metallurgical and Materials Transactions A* **2018**, *49*, 4324-4342, doi:10.1007/s11661-018-4671-7.
27. Furrer, D.U.; Fecht, H.-J. MICROSTRUCTURE AND MECHANICAL PROPERTY DEVELOPMENT IN SUPERALLOY U72OLI. 2001.
28. Schindelin, J.; Arganda-Carreras, I.; Frise, E.; Kaynig, V.; Longair, M.; Pietzsch, T.; Preibisch, S.; Rueden, C.; Saalfeld, S.; Schmid, B.; et al. Fiji: an open-source platform for biological-image analysis. *Nature Methods* **2012**, *9*, 676-682, doi:10.1038/nmeth.2019.
29. Hirel, P. Atomsk: A tool for manipulating and converting atomic data files. *Computer Physics Communications* **2015**, *197*, 212-219, doi:https://doi.org/10.1016/j.cpc.2015.07.012.
30. Groeber, M.A.; Jackson, M.A. DREAM.3D: A Digital Representation Environment for the Analysis of Microstructure in 3D. *Integrating Materials and Manufacturing Innovation* **2014**, *3*, 56-72, doi:10.1186/2193-9772-3-5.
31. Lee, B.-J.; Baskes, M.I. Second nearest-neighbor modified embedded-atom-method potential. *Physical Review B* **2000**, *62*, 8564-8567, doi:10.1103/PhysRevB.62.8564.
32. Etesami, S.A.; Asadi, E. Molecular dynamics for near melting temperatures simulations of metals using modified embedded-atom method. *Journal of Physics and Chemistry of Solids* **2018**, *112*, 61-72, doi:https://doi.org/10.1016/j.jpcs.2017.09.001.
33. Plimpton, S. Fast Parallel Algorithms for Short-Range Molecular Dynamics. *Journal of Computational Physics* **1995**, *117*, 1-19, doi:https://doi.org/10.1006/jcph.1995.1039.
34. Stukowski, A. Visualization and analysis of atomistic simulation data with OVITO–the Open Visualization Tool. *Modelling and Simulation in Materials Science and Engineering* **2009**, *18*, 015012, doi:10.1088/0965-0393/18/1/015012.
35. Stukowski, A.; Albe, K. Extracting dislocations and non-dislocation crystal defects from atomistic simulation data. *Modelling and Simulation in Materials Science and Engineering* **2010**, *18*, 085001, doi:10.1088/0965-0393/18/8/085001.
36. Tsuzuki, H.; Branicio, P.S.; Rino, J.P. Structural characterization of deformed crystals by analysis of common atomic neighborhood. *Computer Physics Communications* **2007**, *177*, 518-523,

doi:10.1016/j.cpc.2007.05.018.

37. Manna, I.; Pabi, S.K.; Gust, W. Discontinuous reactions in solids. *International Materials Reviews* **2001**, *46*, 53-91, doi:10.1179/095066001101528402.

38. Galindo-Nava, E.I.; Connor, L.D.; Rae, C.M.F. On the prediction of the yield stress of unimodal and multimodal γ' Nickel-base superalloys. *Acta Materialia* **2015**, *98*, 377-390, doi:https://doi.org/10.1016/j.actamat.2015.07.048.

39. Jackson, M.P.; Reed, R.C. Heat treatment of UDIMET 720Li: the effect of microstructure on properties. *Materials Science and Engineering: A* **1999**, *259*, 85-97, doi:https://doi.org/10.1016/S0921-5093(98)00867-3.

40. Andersson, J.O.; Helander, T.; Höglund, L.; Shi, P.; Sundman, B. Thermo-Calc & DICTRA, computational tools for materials science. *Calphad* **2002**, *26*, 273-312, doi:https://doi.org/10.1016/S0364-5916(02)00037-8.

41. Guo, Z.L.; Saunders, N.; Miodownik, P.; Schillé, J.P. Modeling Material Properties of Lead-Free Solder Alloys. *Journal of Electronic Materials* **2008**, *37*, 23-31.